ERDC/CHL TR-09-12

Coastal and Hydraulics Laboratory

US Army Corps
of Engineers®
Engineer Research and
Development Center

Navigation Systems Research Program

Locally Conservative, Stabilized Finite Element Methods for a Class of Variable Coefficient Navier-Stokes Equations

C. E. Kees, M. W. Farthing, and M. T. Fong

August 2009

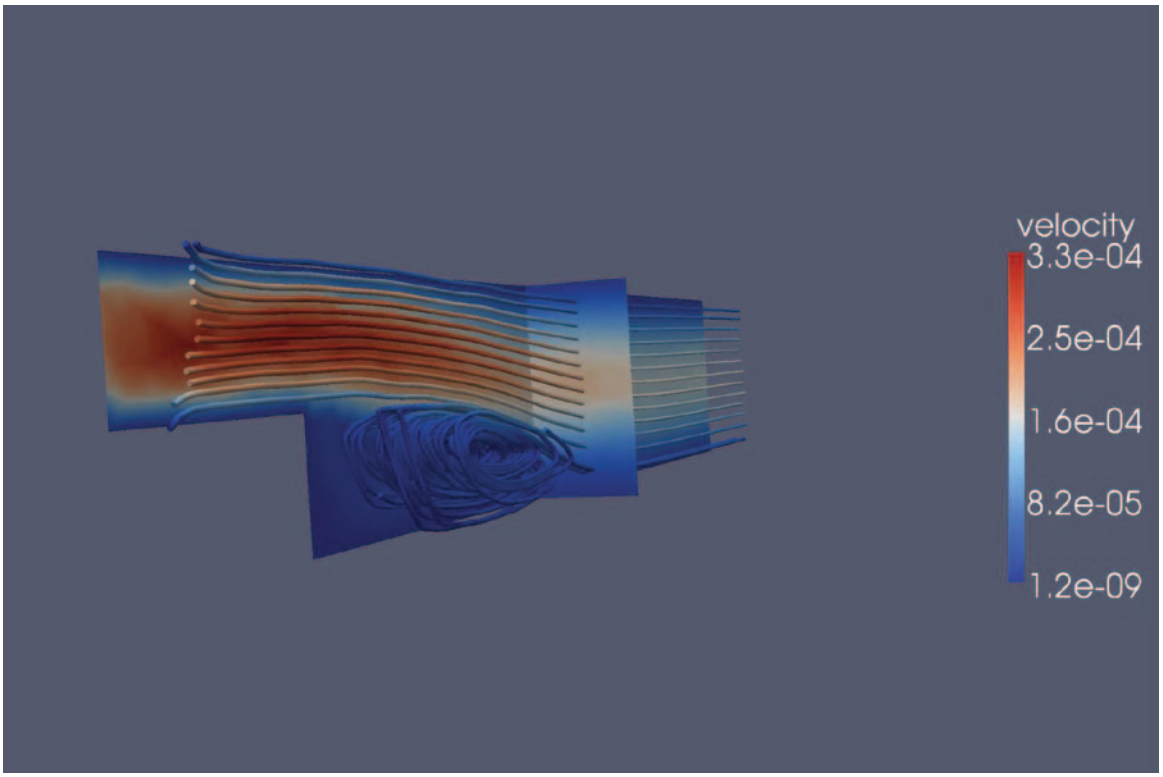

Navigation Systems Research Program

ERDC/CHL TR-09-12
August 2009

Locally Conservative, Stabilized Finite Element Methods for a Class of Variable Coefficient Navier-Stokes Equations

C. E. Kees, M. W. Farthing, and M. T. Fong

Coastal and Hydraulics Laboratory
U.S. Army Engineer Research and Development Center
3909 Halls Ferry Road.
Vicksburg, MS 39180-6199

Final Report

Prepared for U.S. Army Corps of Engineers
Washington, DC 20314-1000

Under Work Unit KHBCGD

Abstract: **Computer simulation of three-dimensional incompressible flow is of interest in many navigation, coastal, and geophysical applications. This report is the the fifth in a series of publications that documents research and development on a state-of-the-art computational modeling capability for fully three-dimensional two-phase fluid flows with vessel/structure interaction in complex geometries (Farthing and Kees, 2008; Kees et al., 2008; Farthing and Kees, 2009; Kees et al., 2009). It is primarily concerned with model verification, often defined as "solving the equations right" (Roache, 1998). Model verification is a critical step on the way to producing reliable numerical models, but it is a step that is often neglected (Oberkampf and Trucano, 2002). Quantitative and qualitative methods for verification also provide metrics for evaluating numerical methods and identifying promising lines of future research.**

Fully-three dimensional flows are often described by the incompressible Navier-Stokes (NS) equations or related model equations such as the Reynolds Averaged Navier Stokes (RANS) equations and Two-Phase Reynolds Averaged Navier-Stokes equations (TPRANS). We will describe spatial and temporal discretization methods for this class of equations and test problems for evaluating the methods and implementations. The discretization methods are based on stabilized continuous Galerkin methods (variational multiscale methods) and discontinous Galerkin methods. The test problems are taken from classical fluid mechanics and well-known benchmarks for incompressible flow codes (Batchelor, 1967; Chorin, 1968; Schäfer et al., 1996; Williams and Baker, 1997; John et al., 2006). We demonstrate that the methods described herein meet three minimal requirements for use in a wide variety of applications: 1) they apply to complex geometries and a range of mesh types; 2) they robustly provide accurate results over a wide range of flow conditions; and 3) they yield qualitatively correct solutions, in particular mass and volume conserving velocity approximations.

Table of Contents

Figures and Tables

Figures

Tables

Preface

This report is a product of the High Fidelity Vessel Effects Work Unit of the Navigation Systems Research Program being conducted at the U.S. Army Engineer Research and Development Center, Coastal and Hydraulics Laboratory.

The report was prepared by Dr. Christopher E. Kees, Dr. Matthew W. Farthing, and Ms. Moira T. Fong under the supervision of Mr. Earl V. Edris, Jr., Chief, Hydrologic Systems Branch. General supervision was provided by Mr. Thomas W. Richardson, Director, CHL; Dr. William D. Martin, Deputy Director, CHL; and Mr. Bruce A. Ebersole, Chief Flood and Storm Protection Division.

Technical advice needed to complete this work was provided by Drs. Stacy E. Howington and Robert S. Bernard, Coastal and Hydraulics Laboratory and Professor Yuri Bazilevs, University of California.

Mr. James E. Clausner, Navigation Systems Program Manager, was the project manager for this effort. Mr. W. Jeff Lillycrop was the Technical Director.

COL Gary E. Johnston was Commander and Executive Director of the Engineer Research and Development Center. Dr. James E. Houston was Director.

This report was typeset by the authors with the LaTeX document preparation system. The report uses the `erdc` document class and `mathgifg` fonts package developed by Dr. Boris Veytsman under the supervision of Mr. Ryan E. North, Geotechnical and Structures Laboratory. The packages are available from `http://ctan.tug.org`.

1 Introduction

Fluid flow in the vicinity of vessels and structures typically becomes quite complex for even moderate flow conditions. Flow conditions are typically characterized by the dimensionless Reynolds number (Re) given by $Re = VL/\nu$ where ν is the kinematic viscosity and V and L characterize the velocity and length scale of a given problem. Figure 1 shows a von Karman vortex street, which is a well-known unsteady flow pattern that can develop behind a cylinder at Re near 100, long before the onset of turbulent flow (Batchelor, 1967). For open channel and coastal modeling, turbulent flows must be approximated using a Reynolds averaging formalism (RANS) or Large Eddy Simulation (LES). Complex averaged velocities develop in these large scale flows regardless (Hutter and Jöhnk, 2004). Fluid flows with a free surface, such as two-phase air/water flow, introduce significantly more complexity because the motion of the free surface (waves) induces additional velocity variation in space and time. The phenomenon that is primarily responsible for generating temporal and spatial complexity in these flows is the interaction of the strongly nonlinear inertial terms with the weak, small-scale viscous terms in the equations. Numerical methods for solving this class of equations must address the destabilizing influence of the inertial (advective) terms in order to obtain accurate solutions.

When simulating turbulent flows, two-phase flows, or turbulent two-phase flows, the velocity field must be used to drive additional transport equations such as the turbulence closure models and the free surface models. If the computed velocity field does not satisfy the continuity equation, then this error leads to incorrect results in these models. The error then propagates to the turbulent and free surface models, which in turn feeds back to the flow model. Attention must be paid to the "compatibility" of numerical solutions, particularly in these cases of coupled flow and transport (Dawson et al., 2004).

In this report we describe finite element discretizations for variable coefficient NS equations that use a multiscale approach to stabilizing the momentum advection term. The approach applies to unstructured meshes and variable order polynomial approximation spaces. Furthermore, we employ a post-processing approach that produces locally conservative ve-

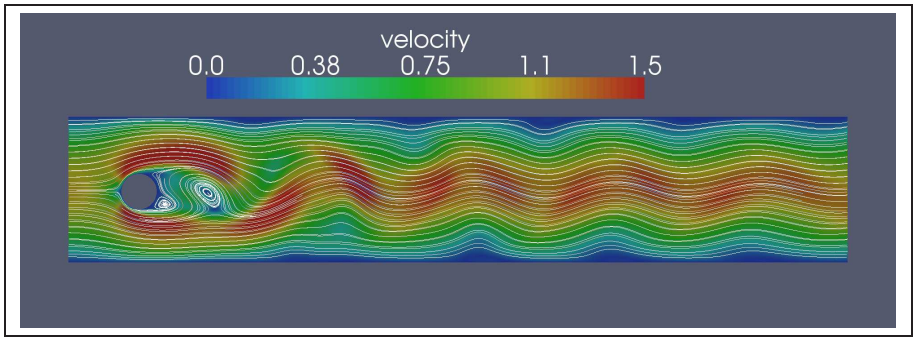

Figure 1. Periodic vortex shedding at Re ≈ 100.

locity approximations as well as an adaptive, variable order, variable step size, temporal discretization. We apply the methods to a range of test problems to verify the implementation and evaluate its accuracy.

The outline of the remainder of this report is as follows. We begin by presenting flow formulations representative of the class of equations for which the discretizations are applicable. Then we present details on the variational multiscale method applied to a representative flow model as well as the time discretization and velocity post-processing. We consider a range of test problems to verify the correctness of the implementation and analyze the results to achieve a better understanding of the robustness, accuracy, and efficiency of the mathematical models. We conclude with some recommendations for future research and development on numerical methods for this class of problems.

2 Formulation

We begin with a physical domain Ω and a time interval $[0, T]$. We write the NS equations for an incompressible, Newtonian fluid in $\Omega \times [0, T]$ as

$$\nabla \cdot \mathbf{v} = 0 \tag{1}$$

$$\frac{\partial \mathbf{v}}{\partial t} + \nabla \cdot \left[\mathbf{v} \otimes \mathbf{v} - \nu(\nabla \mathbf{v} + \nabla \mathbf{v}^t) \right] = \mathbf{g} - \frac{1}{\rho} \nabla p \tag{2}$$

where $\mathbf{v}$ is the velocity, $\mathbf{v} \otimes \mathbf{v}$ is the tensor $\left\{ v_i v_j \right\}, i, j = 1, 2, 3$, ν is the kinematic viscosity, $\mathbf{g}$ is the gravitational acceleration, and ρ is the density. Fully describing either RANS or TPRANS models is beyond the scope of this report and we merely give a representative formulation. A RANS formulation with a first order turbulence closure model can be written as

$$\nabla \cdot \bar{\mathbf{v}} = 0 \tag{3}$$

$$\frac{\partial \bar{\mathbf{v}}}{\partial t} + \nabla \cdot \left[\bar{\mathbf{v}} \otimes \bar{\mathbf{v}} - (\nu + \nu_t)(\nabla \bar{\mathbf{v}} + \nabla \bar{\mathbf{v}}^t) \right] = \mathbf{g} - \frac{1}{\rho} \nabla \left(\bar{p} + \frac{2k}{3} \right) \tag{4}$$

where $\bar{\mathbf{v}}$ and $\bar{p}$ are the Reynold's averaged velocity and pressure, ν_t is the turbulent kinematic viscosity, and k is the turbulent kinetic energy (Hutter and Jöhnk, 2004; Bernard et al., 2007). In this case $\bar{\mathbf{v}}$ and $\bar{p}$ are the unknowns and ν_t and k are also part of the solution arising through the coupling to a turbulence closure model. For an air/water flow, neglecting the effect of surface tension, we can write the TPRANS model equations as

$$\nabla \cdot \bar{\mathbf{v}} = 0 \tag{5}$$

$$\frac{\partial \bar{\mathbf{v}}}{\partial t} + \nabla \cdot \left[\bar{\mathbf{v}} \otimes \bar{\mathbf{v}} - (\nu(\varphi) + \nu_t(\varphi))(\nabla \bar{\mathbf{v}} + \nabla \bar{\mathbf{v}}^t) \right] = \mathbf{g} - \frac{1}{\rho(\varphi)} \nabla \left(\bar{p} + \frac{2k}{3} \right) \tag{6}$$

where φ is a function describing the fluid distribution (e.g. a level set or volume of fluid function). In this case φ is an additional solution variable arising through the coupling of an equation for the fluid-fluid interface.

2.1 Test equation

Since our focus in this report is specifically on spatial discretizations for the flow equation and not on turbulence or free surface modeling, we will focus on the general variable coefficient NS equation

$$\nabla \cdot \mathbf{v} = 0 \tag{7}$$

$$\frac{\partial \mathbf{v}}{\partial t} + \nabla \cdot \left[\mathbf{v} \otimes \mathbf{v} - \nu(\mathbf{x})(\nabla \mathbf{v} + \nabla \mathbf{v}^t) \right] = \mathbf{g} - \frac{1}{\rho(\mathbf{x})} \nabla p \tag{8}$$

Henceforth we will drop the explicit dependence on x.

2.2 Weak formulation

We proceed by defining a standard weak formulation of the NS equation. Boundary conditions are an important and complex aspect of real world modeling that we will not treat fully in this report. Instead we will assume that the boundary of the domain has two partitionings: $\{\partial\Gamma_D^p, \partial\Gamma_N^p\}$ and $\{\Gamma_D^v, \Gamma_N^v\}$ on which the boundary conditions are given as

$$p = p_D \text{ on } \Gamma_D^p \tag{9}$$

$$\mathbf{v} \cdot \mathbf{n} = h_n^p \text{ on } \Gamma_N^p \tag{10}$$

$$\mathbf{v} = \mathbf{v}_D \text{ on } \Gamma_D^v \tag{11}$$

$$\left[\mathbf{v} \otimes \mathbf{v} - \nu(\mathbf{x})(\nabla \mathbf{v} + \nabla \mathbf{v}^t) \right] \cdot \mathbf{n} = \mathbf{h}_N^v \text{ on } \Gamma_N^v \tag{12}$$

Furthermore we assume that $p(\mathbf{x}, 0) = p_0$ and $\mathbf{v}(\mathbf{x}, 0) = \mathbf{v}_0$ are prescribed initial conditions. Since our focus is on numerical methods and test problems, we state an abstract weak formulation of NS problems leaving out almost all rigorous details except those necessary to define the numerical methods. First, we will seek a solutions p and v that are members of spaces of functions $V_T^p(0, T; V^p(\Omega))$, and $V_T^v(0, T; V^v(\Omega))$. In particular this means that $p(t) \in V^p(\Omega)$, $\mathbf{v}(t) \in \mathbf{V}^v(\Omega)$ and that the Dirichlet boundary conditions are incorporated into the definition of $V^p(\Omega)$ and $\mathbf{V}^v(\Omega)$. We say a solution is a weak solution if

$$-\int_\Omega \mathbf{v} \cdot \nabla w^p \, dV = -\int_{\Gamma_N^p} h^p \, dS \quad \forall w^p \in W^p(\Omega) \tag{13}$$

$$\begin{aligned} \int_\Omega \frac{\partial \mathbf{v}}{\partial t} \mathbf{w} - \mathbf{v} \otimes \mathbf{v} \cdot \nabla \mathbf{w}^v \, dV &= -\int_\Omega \nu(\mathbf{x})(\nabla \mathbf{v} + \nabla \mathbf{v}^t) \cdot \nabla \mathbf{w}^v \, dV \\ &\quad + \int_\Omega \left(\mathbf{g} - \frac{1}{\rho(\mathbf{x})} \nabla p \right) \mathbf{w}^v \, dV \\ &\quad - \int_{\Gamma_N^v} \mathbf{h}_N^v \, dS \quad \forall \mathbf{w}^v \in \mathbf{W}^v(\Omega) \end{aligned} \tag{14}$$

where we interpret vector-vector multiplication as component-wise multiplication (i.e. equation 14 is a vector equation). We call $V^p(\Omega)$ the trial space for p and $W^p(\Omega)$ the test space for p.

3 Discrete Approximation

We now define finite dimensional approximation spaces corresponding to the abstract function spaces above. This converts that abstract weak formulation into a problem on the finite dimensional vector space $\mathbb{R}^N$, where N is the number of discrete degrees of freedom.

3.1 Time discretization

First we partition the time interval as $[t_0, t_1, \ldots, t_n, t_{n+1}, \ldots, T]$. Our choice of space for $V_T^v(0, T; V^v(\Omega))$ will be a subspace of the continuous functions, $C_0(0, T; V^v(\Omega))$, including certain polynomials defined on the time discretization. In particular, we will assume that for $n + 1 \geq k$ that v is a Lagrange polynomial in t of the form

$$v(t) = \sum_{k=0}^{n_k} l_k(t) v(t_{n+1-k}, x) \tag{15}$$

where l_k is the Lagrange basis function at t_{n+1-k}. Assuming $v(t_{n+1-k})$ is known for $k > 0$, this implies that

$$\frac{\partial v}{\partial t}(t_{n+1}) = \alpha v(t_{n+1}, x) + \beta \tag{16}$$

where α and β depends on $\{l_k\}$ and $\{v(t_{n+1-k}, x)\}$ for $k = 1, \ldots, n_k$ and l_0. To simplify the notation we define

$$D_t v_{n+1}(x) := \alpha v(t_{n+1}, x) + \beta \tag{17}$$

This approximation converts the initial-boundary value problem into a sequence of boundary value problems at $t_1, t_2, \ldots, T$. Dropping the time subscript $n + 1$ we write the weak formulation of the boundary value problem as

$$-\int_\Omega v \cdot \nabla w^p dV = -\int_{\Gamma_N^p} h^p dS \quad \forall w^p \in W^p(\Omega) \tag{18}$$

$$\begin{aligned} \int_\Omega D_t v w - v \otimes v \cdot \nabla w^v dV &= -\int_\Omega \nu(x)(\nabla v + \nabla v^t) \cdot \nabla w^v dV \\ &\quad + \int_\Omega \left(g - \frac{1}{\rho(x)} \nabla p \right) w^v dV \\ &\quad - \int_{\Gamma_N^v} h_N^v dS \quad \forall w^v \in W^v(\Omega) \end{aligned} \tag{19}$$

3.2 Multiscale formulation

We now build an approximate weak formulation in time using the multiscale formalism of (Hughes, 1995). Let $\mathbf{M}^h$ be a simplicial mesh on Ω in $\mathbb{R}^{n_d}$, $n_d = 2, 3$, containing N_e elements, $\{\Omega_e\}, e = 1, \ldots, N_e$, N_f faces, $\{\gamma_f\}, f = 1, \ldots, N_f$, and N_n nodes, $\{x_n\}, n = 1, \ldots, N_n$. The collection of faces in the domain interior is denoted Γ_I. We also assume that the intersection of elements $\Omega_e, \Omega_{e'} \in \mathbf{M}^h$ is either empty, a unique $\gamma_f \in \Gamma_I$, an edge (for $\mathbb{R}^3$), or a point. The diameter of Ω_e is h_e and its unit outer normal is written n_e.

Consider test and trial spaces V and W. The basic idea of a multiscale method is to split V and W into resolved and unresolved scales using direct sum decompositions

$$V = V_h \oplus \delta V \tag{20}$$

$$W = W_h \oplus \delta W \tag{21}$$

For this work V_h and W_h are the continuous, piecewise polynomial spaces of the classical Galerkin finite element method:

$$V_h = \{v_h \in V \cap C^0(\bar{\Omega}) : v_h|_{\Omega_e} \in P^k(\Omega_e)\} \tag{22}$$

$$W_h = \{w_h \in W \cap C^0(\bar{\Omega}) : w_h|_{\Omega_e} \in P^k(\Omega_e)\} \tag{23}$$

while δV and δW remain infinite dimensional. We will consider $k = 1$ or $k = 2$ and the standard extensions of these spaces to spaces of vector valued functions written as $\mathbf{V}_h$ and $\mathbf{W}_h$.

With this decomposition for V^p and V^v, the solution is written uniquely as $p = p_h + p'$ and $v = v_h + v'$. After some manipulation and approximation (Hughes, 1995), we obtain the weak formulation

$$-\int_\Omega v_h \cdot \nabla w_h^p dV + \int_\Omega v' L_{v,p}^* w_h^p dV = -\int_{\Gamma_N^p} h^p dS \quad \forall w_h^p \in W_h^p(\Omega) \tag{24}$$

$$\begin{aligned}\int_\Omega D_t v_h w_h - \left[v_h \otimes v_h - \nu(\nabla v_h + \nabla v_h^t)\right] \cdot \nabla w_h^v dV + \int_\Omega v' L_{v,v}^* w_h^v dV \\ = \int_\Omega \left(g - \frac{1}{\rho}\nabla p_h\right) w_h^v dV \\ + \int_\Omega p' L_{p,v}^* w_h^v dV \\ - \int_{\Gamma_N^v} h_N^v dS \quad \forall w_h^v \in W_h^v(\Omega)\end{aligned} \tag{25}$$

where

$$L^{*}_{v,p} w^{p}_{h} = -\nabla w^{p}_{h} \quad (26)$$

$$L^{*}_{v,v} w^{v}_{h} = -\nabla w^{v}_{h} v_{n} - \nu \Delta w^{v}_{h} \quad (27)$$

$$L^{*}_{p,v} w^{v}_{h} = \left(\frac{\partial w_{h,x}}{\partial x}, \frac{\partial w_{h,y}}{\partial y}, \frac{\partial w_{h,z}}{\partial z}\right)^{t} \quad (28)$$

The operators $L^{*}_{v,p}$ and $L^{*}_{p,v}$ are the adjoint operators corresponding to the divergence and pressure gradient operators. The operator $L^{*}_{v,v}$ is the adjoint of the operator obtained by linearizing the first term in 25 and assuming that $D_t w_h$ and $\nabla \cdot v$ are zero.

3.3 Algebraic sub-grid scale approximation

To obtain a closed set of equations for p_h, v_h we need approximations for p' and v'. We use the standard Algebraic-Sub-Grid Scale (ASGS) approximations given by

$$p' = -\tau_p R_p \quad (29)$$

$$v' = -\tau_v R_v \quad (30)$$

where

$$\tau_p = 4\nu + 2\rho \|v_{h,n-1}\| \hat{h} + |D'_t| \hat{h}^2 \quad (31)$$

$$\tau_v = \frac{1}{\frac{4\nu}{\hat{h}^2} + \frac{2\rho \|v_{h,n-1}\|}{\hat{h}} + |D'_t|} \quad (32)$$

and

$$R_p = \nabla \cdot v_h \quad (33)$$

$$R_v = D_t v_h + v_{h,n-1} \cdot \nabla v_h - \nu \Delta v_h - g + \frac{1}{\rho} \nabla p \quad (34)$$

$$\hat{h} = \begin{cases} h_e & k = 1 \\ h_e / 2 & k = 2 \end{cases} \quad (35)$$

3.4 Velocity post-processing

Quite often a velocity approximation along the boundaries of the mesh elements is required as input to other models such as chemical species

transport and particle tracking. One shortcoming of the finite element approximations above is that the condition $\nabla \cdot \mathbf{v} = 0$ may not be locally conservative, i.e.

$$\int_{\partial\Omega_e} \mathbf{v_h} \cdot \mathbf{n} dS \neq 0 \tag{36}$$

For this reason we post-process $\mathbf{v}$ to obtain a new velocity $\hat{\mathbf{v}}$ in the space $\hat{\mathbf{V}}$ defined by

$$\hat{\mathbf{V}}(\Omega) = \left\{ \hat{\mathbf{v}} \in C_0(\Omega) : \hat{\mathbf{v}}|_{\Omega_e} \in (P^0(\Omega_e))^2 \oplus (\mathbf{x}P^0(\Omega_e)) \right\} \tag{37}$$

The space $\hat{\mathbf{V}}(\Omega)$ is the velocity space for the well-known Raviart-Thomas space of order zero (RT0). The post-processed velocity satisfies equation 36 up to the accuracy of the nonlinear solver and the error is

$$\left\| \hat{\mathbf{v}} - \mathbf{v}^* \right\|_{(L_2(\Omega))^{n_d}} \leq Ch \tag{38}$$

for some constant C depending on the exact solution $\mathbf{v}^*$ but independent of the maximum element diameter h. This approach was originally presented in (Larson and Niklasson, 2004) and the implementation in this work was evaluated on a variety of variable coefficient test problems and unstructured meshes in (Kees et al., 2008).

3.5 Additional details

The discretization above yields a system of nonlinear algebraic equations at each time step. To solve these systems in the time-dependent case we used Newton's method. In steady state cases we used either Newton's method or Pseudo-transience continuation (Knoll and McHugh, 1998; Farthing et al., 2003). The 2D simulations were run on a MacPro 2x3 GHz Quad-Core Intel Xeon processor with 16 GB of memory. On this system linear systems were solved using the SuperLU (serial) sparse direct solver (Demmel et al., 1999). The 3D simulations were run on 32 or 64 cores of a Dell Linux Cluster with 1955 2x2.66 GHz Quad-Core Intel Xeon nodes with 8GB of memory. On this platform we used the SPOOLES parallel sparse direct solver (Ashcraft and Grimes, 1999) via the PETSc framework (Balay et al., 2001, 2004, 1997).

4 Model Verification

4.1 Plane Poiseuille and Couette Flow

First we consider steady-state flow between two parallel plates of infinite extent, where the flow is driven by the movement of the top plate and/or an externally applied pressure gradient. Assuming the Z-axis is normal to the plates and that the flow and pressure gradient are alligned with the X-axis, the solution to the incompressible NS equations in this case is

$$\mathbf{u}^*(\mathbf{Z}) = \frac{\mathbf{ZU}}{\mathbf{L_Z}} + \frac{1}{2\boldsymbol{\mu}}\frac{\partial \mathbf{p}^*}{\partial \mathbf{X}}\mathbf{Z}(\mathbf{Z}-\mathbf{L_Z}) \quad \mathbf{V} = \mathbf{W} = 0 \tag{39}$$

$$\mathbf{p}^*(\mathbf{X}) = \frac{\partial \mathbf{p}^*}{\partial \mathbf{X}}\mathbf{X} + \mathbf{p}_0 \tag{40}$$

where H is the distance between the plates, $(\mathbf{U}, 0, 0)$ is the velocity of the top plate relative to the bottom plate and $\mathbf{p}_0$ is an arbitrary constant. To use this solution for model verification on a finite domain we consider a translated and rotated coordinate system $(\mathbf{x}, \mathbf{y}, \mathbf{z})$ and a rectangular region between the plates given by $\Omega = [0, \mathbf{L_x}] \times [0, \mathbf{L_y}] \times [0, \mathbf{L_z}]$. In particular we use

$$\mathbf{X} = \mathbf{x} \cdot \mathbf{n_v} \tag{41}$$

$$\mathbf{Z} = \mathbf{x} \cdot \mathbf{n_p} - \mathbf{Z_s} \tag{42}$$

$$\mathbf{n_p} = (\cos(\theta_p)\sin(\varphi_p), \sin(\theta_p)\sin(\varphi_p), \cos(\varphi_p))^t \tag{43}$$

$$\mathbf{n_v} = (\cos(\theta_v)\sin(\varphi_v), \sin(\theta_v)\sin(\varphi_v), \cos(\varphi_v))^t \tag{44}$$

To verify the spatial discretizations we solved this problem with four levels of mesh refinement choosing $\theta_p, \varphi_p, \theta_v, \varphi_v$ so that flow is skew to the grid. The results for 2D with

θ_p	φ_p	θ_v	φ_v	Z_s
$2\pi/3$	$\pi/2$	$\pi/6$	$\pi/2$	-1/2

and 3D with

Table 1. Grid refinement study for 2D Poiseuille problem.

h	$\|\mathbf{p}-\mathbf{p}^*\|_{L_2(\Omega)}$	$\|\mathbf{u}-\mathbf{u}^*\|_{L_2(\Omega)}$	$\|\mathbf{v}-\mathbf{v}^*\|_{L_2(\Omega)}$
$\frac{\partial \mathbf{p}}{\partial \mathbf{X}} = 0, \mathbf{k} = 1$			
0.5	1.53×10^{-8}	5.82×10^{-12}	7.52×10^{-12}
0.25	9.66×10^{-10}	7.03×10^{-13}	1.03×10^{-12}
0.125	6.97×10^{-11}	1.12×10^{-13}	4.80×10^{-14}
0.0625	5.17×10^{-12}	8.43×10^{-15}	7.65×10^{-15}
$\frac{\partial \mathbf{p}}{\partial \mathbf{X}} = -1, \mathbf{k} = 1$			
0.5	1.01×10^{5}	1.17×10^{1}	6.71×10^{0}
0.25	1.16×10^{5}	3.09×10^{0}	1.69×10^{0}
0.125	3.25×10^{4}	7.37×10^{-1}	4.64×10^{-1}
0.0625	8.97×10^{3}	1.78×10^{-1}	1.29×10^{-1}
$\frac{\partial \mathbf{p}}{\partial \mathbf{X}} = 0, \mathbf{k} = 2$			
0.5	2.77×10^{-9}	2.33×10^{-12}	2.64×10^{-12}
0.25	4.02×10^{-10}	7.81×10^{-13}	4.29×10^{-13}
0.125	9.58×10^{-11}	1.21×10^{-13}	8.85×10^{-14}
0.0625	1.16×10^{-11}	2.03×10^{-14}	1.10×10^{-14}
$\frac{\partial \mathbf{p}}{\partial \mathbf{X}} = -1, \mathbf{k} = 2$			
0.5	6.66×10^{-9}	4.10×10^{-14}	2.88×10^{-14}
0.25	5.49×10^{-9}	5.34×10^{-14}	2.61×10^{-14}
0.125	1.11×10^{-8}	8.80×10^{-14}	6.74×10^{-14}
0.0625	2.12×10^{-8}	1.72×10^{-13}	1.33×10^{-13}

θ_p	φ_p	θ_v	φ_v	Z_s
$\pi/6$	$\pi/6$	$\pi/3$	$\pi/6$	0

are given in Figures 1 and 2. The quadratic finite element approximation ($\mathbf{k} = 2$) is accurate to within the nonlinear solver tolerance of 1.0×10^{-7} in all cases, demonstrating that it is essentially able to represent the true solution exactly. The linear finite element approximation ($\mathbf{k} = 1$) is essentially exact when the solution is linear ($\frac{\partial \mathbf{p}}{\partial \mathbf{X}} = 0$) and demonstrates quadratic convergence, which is consistent with the theoretical a priori error estimates for smooth solutions.

4.2 Vortex decay

This time-dependent problem was originally described in (Chorin, 1968) and was used to study time discretizations for the NS equations in (John et al., 2006). The flow domain is again $\Omega = [0,1]\times[0,1]$. The analytical

Table 2. Grid refinement study for 3D Poiseuille problem.

h	$\|p - p^*\|_{L_2(\Omega)}$	$\|u - u^*\|_{L_2(\Omega)}$	$\|v - v^*\|_{L_2(\Omega)}$	$\|w - w^*\|_{L_2(\Omega)}$
$\frac{\partial p}{\partial x} = 0, k = 1$				
0.5	3.28×10^{-9}	3.94×10^{-12}	1.92×10^{-12}	6.30×10^{-12}
0.25	4.34×10^{-10}	1.18×10^{-12}	1.90×10^{-12}	4.21×10^{-13}
0.125	1.18×10^{-10}	2.04×10^{-13}	2.61×10^{-13}	1.89×10^{-13}
0.0625	3.12×10^{-11}	9.59×10^{-14}	1.47×10^{-13}	7.21×10^{-14}
$\frac{\partial p}{\partial x} = -1, k = 1$				
0.5	4.02×10^{5}	1.69×10^{1}	2.91×10^{1}	1.75×10^{1}
0.25	2.93×10^{5}	4.55×10^{0}	7.70×10^{0}	4.87×10^{0}
0.125	9.51×10^{4}	1.12×10^{0}	1.90×10^{0}	1.41×10^{0}
0.0625	2.66×10^{4}	2.80×10^{-1}	4.70×10^{-1}	3.85×10^{-1}
$\frac{\partial p}{\partial x} = 0, k = 2$				
0.5	8.89×10^{-9}	1.95×10^{-11}	3.87×10^{-11}	3.87×10^{-11}
0.25	2.74×10^{-9}	8.66×10^{-12}	1.53×10^{-11}	1.10×10^{-11}
0.125	7.69×10^{-10}	1.32×10^{-12}	3.18×10^{-12}	2.10×10^{-12}
0.0625	1.08×10^{-10}	3.05×10^{-13}	4.98×10^{-13}	3.34×10^{-13}
$\frac{\partial p}{\partial x} = -1, k = 2$				
0.5	5.80×10^{-9}	3.41×10^{-14}	5.90×10^{-14}	4.79×10^{-14}
0.25	9.92×10^{-9}	4.40×10^{-14}	7.18×10^{-14}	6.30×10^{-14}
0.125	2.74×10^{-8}	1.06×10^{-13}	2.80×10^{-13}	1.12×10^{-13}
0.0625	2.11×10^{-8}	1.12×10^{-13}	2.19×10^{-13}	1.11×10^{-13}

solution is given by

$$p^* = -\frac{1}{4}(\cos(2n_v\pi x)\sin(2n_v\pi y))\exp(-4n_v^2\pi^2 t/Re) \quad (45)$$

$$u^* = -\cos(n_v\pi x)\sin(n_v\pi y)\exp(-2n_v^2\pi^2 t/Re) \quad (46)$$

$$v^* = \sin(n_v\pi x)\cos(n_v\pi y)\exp(-2n_v^2\pi^2 t/Re) \quad (47)$$

and $Re = 1/\nu$. We use this solution to provide non-homogeneous Dirichlet boundary conditions and initial conditions for all variables. The solution is an array of $n_V \times n_V$ vortices with alternating rotation which decay in time exponentially at a rate controlled by Re. In Tables 3 and 4 we present errors for refinement in space and time for2×2 vortices at $Re = 1$ and 1×10^6. In a three cases the high Re runs failed (denoted by an X) due to repeated reduction of the time step in cases with tol $\leq 1.0 \times 10^{-4}$. This failure mode occurs because the ASGS approximation becomes badly scaled for small time steps (Bazilevs et al., 2007). Subgrid error approximations that are valid for small timesteps is an open area of research, but safeguarding against small time steps (or choosing temporal error tolerances appropriate for the given mesh) should be

sufficient for most applications where a time step on the order of the advective Courant-Friedrich-Levy condition is appropriate.

4.3 Lid driven cavity

The flow domain is $\Omega = [0, a] \times [0, b] \times [0, c]$. The boundary conditions are given by

$$\begin{aligned} \mathbf{v} &= (U, V, 0) \quad \text{on } z = c, 0 < x < a, 0 < y < b \\ \mathbf{v} &= 0 \quad \text{on } x = 0, a, y = 0, b, z = 0 \\ p(a/2, b/2, c) &= 0 \end{aligned} \tag{48}$$

This problem has no analytical solution and exhibits a wide range of behavior depending on the Re. There is a discontinuity in the velocity at the boundary along the upper edges of the cavity (corners in 2D). The discontinuity reduces the regularity of the solution and consequently produces a reduction in the asymptotic order of convergence. Nevertheless, it is a standard verification problem, and a great deal is known about the structure of solutions (Bassi et al., 2006; Erturk et al., 2005). In Figure 5 we present the results of a grid refinement study with four levels of mesh refinement using the fourth level as the "exact" solution. This measure of error is not accurate enough to compare two methods of different orders. The L_2 error estimates are shown to be decreasing monotonically but clearly the order of convergence is less than the quadratic and cubic rates predicted by the theory for smooth solutions. The streamlines for the driven cavity in 2D and 3D are given in Figures 2 - 4. The structure of the flows is in close agreement with previous numerical studies, in particular the detailed high Re studies in (Erturk et al., 2005).

4.4 Backward facing step

In this problem we consider flow over a square step at the lower left hand edge of the domain. We can describe the step as

$$\Omega_s = \{x : 0 < x < a_s, 0 < y < b, 0 < z < c_s\} \tag{49}$$

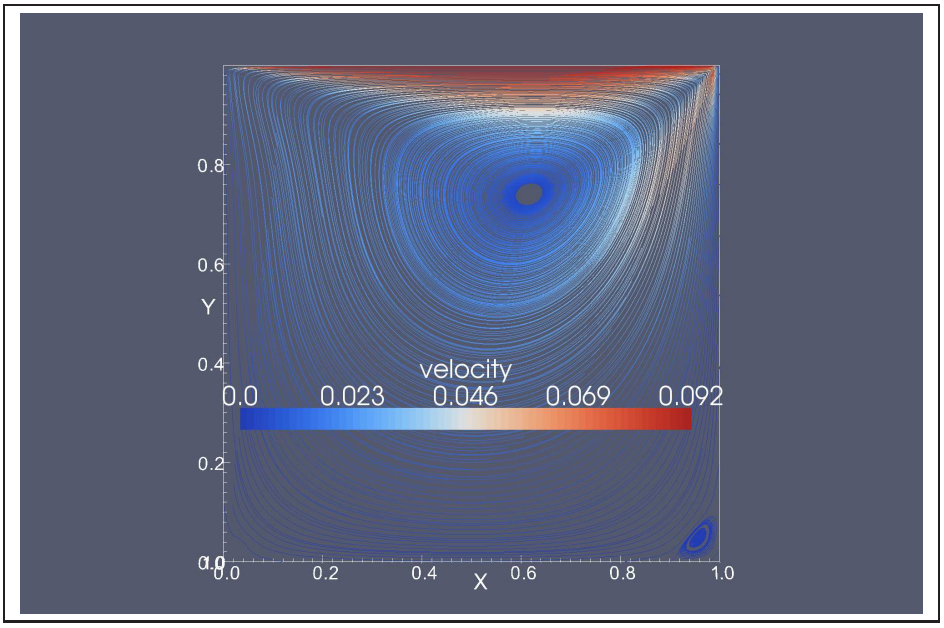

Figure 2. Lid driven cavity in 2D at Re = 100.

the flow domain is then $\Omega = [0, a] \times [0, b] \times [0, c] \bigcap \Omega_s^c$. The boundary conditions are given by

$$\begin{aligned}
u &= z(z-c)\frac{6v^2 Re}{c_s^3} && \text{on } x = 0 \\
v &= w = 0 && \text{on } x = 0 \\
v &= 0 && \text{on } \partial\Omega_s, z = 0, c \\
v \cdot n &= 0 && \text{on } \partial\Omega_s, z = 0, c \\
v(x, 0, z) &= v(x, b, z) && \\
p(x, 0, z) &= p(x, b, z) && \\
p &= 0 && \text{on } x = a \\
-v(x)(\nabla v + \nabla v^t) \cdot n &= 0 && \text{on } x = a
\end{aligned} \tag{50}$$

This problem has been the focus of much experimental and numerical study, and we will derive the details of the test problem from the experimental work in (Armaly et al., 1983) and one of the subsequent numerical studies (Williams and Baker, 1997). The dimensions of the domain are given by

a_s	c_s	a	c
5	4.9	155	10.1

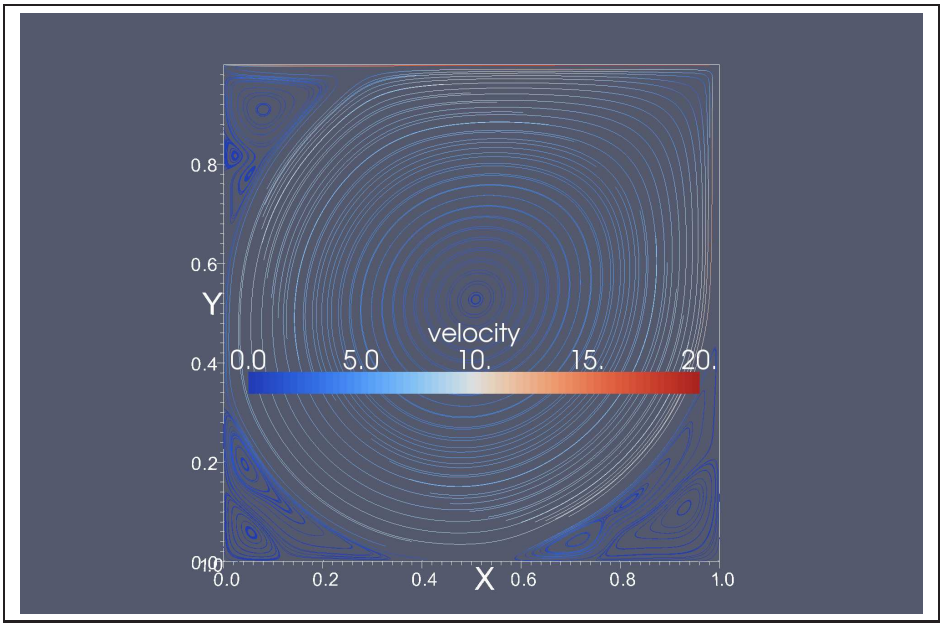

Figure 3. Lid driven cavity in 2D at Re = 20000.

The recirculation length of the primary vortex for Re= $100 - 800$ is given in Figure 5, which is in close agreement with (Williams and Baker, 1997). Examples of the vortex structure in 2D and 3D are given in Figures 6 and 7.

4.5 Flow past a cylinder

We consider flow around a cylinder of radius R, oriented along the y-axis. The cylinder can be described implicitly by

$$\Omega_s = \left\{ \mathbf{x} : \sqrt{(x - x_c)^2 + (z - z_c)^2} < r \right\} \tag{51}$$

the flow domain is the $\Omega = [0, a] \times [0, b] \times [0, c] \bigcap \Omega_s^c$ where Ω_s^c is the complement of Ω_s. The boundary conditions are given by

$$\begin{aligned}
u &= \sin\left(\frac{\pi t}{8}\right)\frac{6z(c-z)}{c^2} && \text{on } x = 0 \\
u &= v = 0 && \text{on } x = 0 \\
v &= 0 && \text{on } \partial\Omega_s, z = 0, c \\
v \cdot 0 &= 0 && \text{on } y = 0, b \\
-\nu(x)(\nabla v + \nabla v^t) \cdot n &= 0 && \text{on } x = a, y = 0, b \\
p &= 0 && \text{on } x = a
\end{aligned} \tag{52}$$

This problem has no analytical solution and exhibits a wide range of behavior depending on Re. The variation in the lift coefficient is shown in

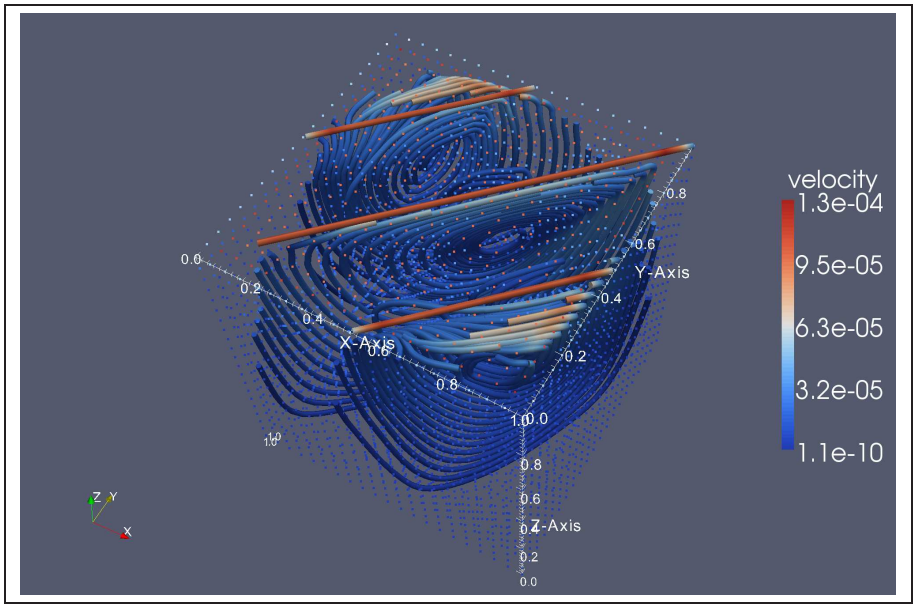

Figure 4. Lid driven cavity in 3D at Re = 100.

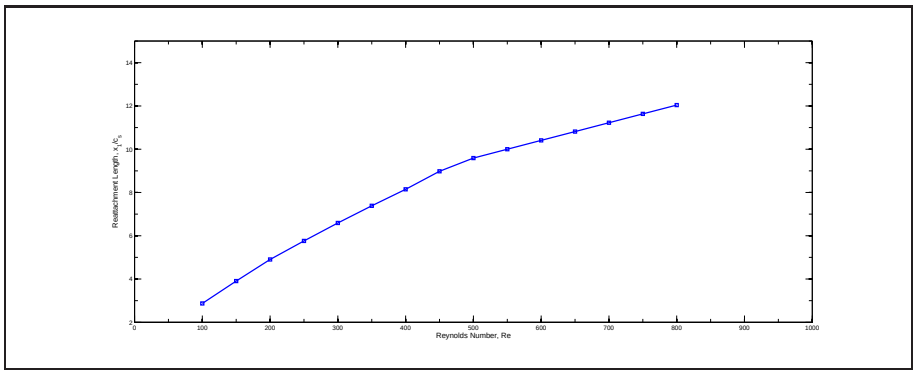

Figure 5. Primary reattachment length versus Re.

Figure 8, which closely matches prior results studying higher-order time discretizations (John et al., 2006).

Table 3. Grid refinement study for vortex decy problem Re = 1.

tol	1.0×10^{-2}	1.0×10^{-3}	1.0×10^{-4}	1.0×10^{-5}
$\mathbf{h} = 0.1, \mathbf{k} = 1$				
$\|\mathbf{p} - \mathbf{p}^*\|_{L_2(\Omega)}$	2.01×10^{-1}	2.49×10^{-1}	2.59×10^{-1}	2.54×10^{-1}
$\|\mathbf{u} - \mathbf{u}^*\|_{L_2(\Omega)}$	4.59×10^{-2}	5.64×10^{-2}	5.96×10^{-2}	5.94×10^{-2}
$\|\mathbf{v} - \mathbf{v}^*\|_{L_2(\Omega)}$	4.59×10^{-2}	5.63×10^{-2}	5.95×10^{-2}	5.94×10^{-2}
$\mathbf{h} = 0.05, \mathbf{k} = 1$				
$\|\mathbf{p} - \mathbf{p}^*\|_{L_2(\Omega)}$	1.22×10^{-1}	8.29×10^{-2}	1.83×10^{-1}	1.15×10^{-1}
$\|\mathbf{u} - \mathbf{u}^*\|_{L_2(\Omega)}$	1.09×10^{-2}	1.19×10^{-2}	1.74×10^{-2}	1.72×10^{-2}
$\|\mathbf{v} - \mathbf{v}^*\|_{L_2(\Omega)}$	1.09×10^{-2}	1.19×10^{-2}	1.73×10^{-2}	1.72×10^{-2}
$\mathbf{h} = 0.025, \mathbf{k} = 1$				
$\|\mathbf{p} - \mathbf{p}^*\|_{L_2(\Omega)}$	2.33×10^{-1}	5.28×10^{-2}	4.45×10^{-2}	3.84×10^{-2}
$\|\mathbf{u} - \mathbf{u}^*\|_{L_2(\Omega)}$	1.10×10^{-2}	3.14×10^{-3}	4.37×10^{-3}	4.39×10^{-3}
$\|\mathbf{v} - \mathbf{v}^*\|_{L_2(\Omega)}$	1.10×10^{-2}	3.14×10^{-3}	4.37×10^{-3}	4.39×10^{-3}
$\mathbf{h} = 0.0125, \mathbf{k} = 1$				
$\|\mathbf{p} - \mathbf{p}^*\|_{L_2(\Omega)}$	3.09×10^{-1}	2.79×10^{-2}	1.74×10^{-2}	1.19×10^{-2}
$\|\mathbf{u} - \mathbf{u}^*\|_{L_2(\Omega)}$	1.29×10^{-2}	2.46×10^{-3}	1.03×10^{-3}	1.06×10^{-3}
$\|\mathbf{v} - \mathbf{v}^*\|_{L_2(\Omega)}$	1.29×10^{-2}	2.46×10^{-3}	1.03×10^{-3}	1.06×10^{-3}
$\mathbf{h} = 0.1, \mathbf{k} = 2$				
$\|\mathbf{p} - \mathbf{p}^*\|_{L_2(\Omega)}$	1.49×10^{-1}	8.68×10^{-2}	6.90×10^{-2}	5.85×10^{-2}
$\|\mathbf{u} - \mathbf{u}^*\|_{L_2(\Omega)}$	1.33×10^{-2}	7.48×10^{-3}	1.22×10^{-3}	1.27×10^{-3}
$\|\mathbf{v} - \mathbf{v}^*\|_{L_2(\Omega)}$	1.33×10^{-2}	7.49×10^{-3}	1.23×10^{-3}	1.27×10^{-3}
$\mathbf{h} = 0.05, \mathbf{k} = 2$				
$\|\mathbf{p} - \mathbf{p}^*\|_{L_2(\Omega)}$	2.41×10^{-1}	1.88×10^{-2}	1.52×10^{-2}	1.70×10^{-2}
$\|\mathbf{u} - \mathbf{u}^*\|_{L_2(\Omega)}$	1.36×10^{-2}	5.48×10^{-3}	1.00×10^{-3}	1.59×10^{-4}
$\|\mathbf{v} - \mathbf{v}^*\|_{L_2(\Omega)}$	1.36×10^{-2}	5.48×10^{-3}	1.00×10^{-3}	1.58×10^{-4}
$\mathbf{h} = 0.025, \mathbf{k} = 2$				
$\|\mathbf{p} - \mathbf{p}^*\|_{L_2(\Omega)}$	3.07×10^{-1}	1.88×10^{-2}	7.23×10^{-3}	3.66×10^{-3}
$\|\mathbf{u} - \mathbf{u}^*\|_{L_2(\Omega)}$	1.36×10^{-2}	6.53×10^{-3}	8.94×10^{-5}	3.84×10^{-5}
$\|\mathbf{v} - \mathbf{v}^*\|_{L_2(\Omega)}$	1.36×10^{-2}	6.53×10^{-3}	8.92×10^{-5}	3.80×10^{-5}
$\mathbf{h} = 0.0125, \mathbf{k} = 2$				
$\|\mathbf{p} - \mathbf{p}^*\|_{L_2(\Omega)}$	3.43×10^{-1}	1.51×10^{-2}	9.08×10^{-3}	9.15×10^{-4}
$\|\mathbf{u} - \mathbf{u}^*\|_{L_2(\Omega)}$	1.36×10^{-2}	6.85×10^{-3}	9.52×10^{-5}	4.13×10^{-5}
$\|\mathbf{v} - \mathbf{v}^*\|_{L_2(\Omega)}$	1.36×10^{-2}	6.85×10^{-3}	9.51×10^{-5}	4.13×10^{-5}

Table 4. Grid refinement study for vortex decy problem Re = 1×10^6.

tol	1.0×10^{-2}	1.0×10^{-3}	1.0×10^{-4}	1.0×10^{-5}
$\mathbf{h} = 0.1, \mathbf{k} = 1$				
$\|\mathbf{p} - \mathbf{p}^*\|_{L_2(\Omega)}$	1.74×10^5	2.24×10^5	2.33×10^5	2.30×10^5
$\|\mathbf{u} - \mathbf{u}^*\|_{L_2(\Omega)}$	4.40×10^{-2}	5.44×10^{-2}	5.76×10^{-2}	5.74×10^{-2}
$\|\mathbf{v} - \mathbf{v}^*\|_{L_2(\Omega)}$	4.40×10^{-2}	5.44×10^{-2}	5.76×10^{-2}	5.74×10^{-2}
$\mathbf{h} = 0.05, \mathbf{k} = 1$				
$\|\mathbf{p} - \mathbf{p}^*\|_{L_2(\Omega)}$	1.16×10^5	7.54×10^4	**X**	1.09×10^5
$\|\mathbf{u} - \mathbf{u}^*\|_{L_2(\Omega)}$	1.07×10^{-2}	1.15×10^{-2}	**X**	1.68×10^{-2}
$\|\mathbf{v} - \mathbf{v}^*\|_{L_2(\Omega)}$	1.07×10^{-2}	1.15×10^{-2}	**X**	1.68×10^{-2}
$\mathbf{h} = 0.025, \mathbf{k} = 1$				
$\|\mathbf{p} - \mathbf{p}^*\|_{L_2(\Omega)}$	2.33×10^5	5.15×10^4	4.35×10^4	3.68×10^4
$\|\mathbf{u} - \mathbf{u}^*\|_{L_2(\Omega)}$	1.10×10^{-2}	3.10×10^{-3}	4.31×10^{-3}	4.33×10^{-3}
$\|\mathbf{v} - \mathbf{v}^*\|_{L_2(\Omega)}$	1.10×10^{-2}	3.10×10^{-3}	4.31×10^{-3}	4.33×10^{-3}
$\mathbf{h} = 0.0125, \mathbf{k} = 1$				
$\|\mathbf{p} - \mathbf{p}^*\|_{L_2(\Omega)}$	3.08×10^5	2.76×10^4	1.74×10^4	1.01×10^4
$\|\mathbf{u} - \mathbf{u}^*\|_{L_2(\Omega)}$	1.29×10^{-2}	2.47×10^{-3}	1.03×10^{-3}	1.05×10^{-3}
$\|\mathbf{v} - \mathbf{v}^*\|_{L_2(\Omega)}$	1.29×10^{-2}	2.47×10^{-3}	1.03×10^{-3}	1.05×10^{-3}
$\mathbf{h} = 0.1, \mathbf{k} = 2$				
$\|\mathbf{p} - \mathbf{p}^*\|_{L_2(\Omega)}$	1.51×10^5	8.70×10^4	5.77×10^4	**X**
$\|\mathbf{u} - \mathbf{u}^*\|_{L_2(\Omega)}$	1.34×10^{-2}	7.51×10^{-3}	1.22×10^{-3}	**X**
$\|\mathbf{v} - \mathbf{v}^*\|_{L_2(\Omega)}$	1.34×10^{-2}	7.51×10^{-3}	1.22×10^{-3}	**X**
$\mathbf{h} = 0.05, \mathbf{k} = 2$				
$\|\mathbf{p} - \mathbf{p}^*\|_{L_2(\Omega)}$	2.42×10^5	1.69×10^4	1.46×10^4	**X**
$\|\mathbf{u} - \mathbf{u}^*\|_{L_2(\Omega)}$	1.36×10^{-2}	5.31×10^{-3}	9.70×10^{-4}	**X**
$\|\mathbf{v} - \mathbf{v}^*\|_{L_2(\Omega)}$	1.36×10^{-2}	5.31×10^{-3}	9.70×10^{-4}	**X**
$\mathbf{h} = 0.025, \mathbf{k} = 2$				
$\|\mathbf{p} - \mathbf{p}^*\|_{L_2(\Omega)}$	3.07×10^5	1.80×10^4	7.06×10^3	3.50×10^3
$\|\mathbf{u} - \mathbf{u}^*\|_{L_2(\Omega)}$	1.36×10^{-2}	6.51×10^{-3}	8.83×10^{-5}	4.12×10^{-5}
$\|\mathbf{v} - \mathbf{v}^*\|_{L_2(\Omega)}$	1.36×10^{-2}	6.51×10^{-3}	8.83×10^{-5}	4.12×10^{-5}
$\mathbf{h} = 0.0125, \mathbf{k} = 2$				
$\|\mathbf{p} - \mathbf{p}^*\|_{L_2(\Omega)}$	3.43×10^5	1.45×10^4	9.20×10^3	8.65×10^2
$\|\mathbf{u} - \mathbf{u}^*\|_{L_2(\Omega)}$	1.36×10^{-2}	6.86×10^{-3}	9.54×10^{-5}	4.13×10^{-5}
$\|\mathbf{v} - \mathbf{v}^*\|_{L_2(\Omega)}$	1.36×10^{-2}	6.86×10^{-3}	9.54×10^{-5}	4.13×10^{-5}

Table 5. 2D lid driven cavity at Re = 100,400,1000.

h	$\|\mathbf{p}-\mathbf{p}^4\|_{L_2(\Omega)}$	$\|\mathbf{u}-\mathbf{u}^4\|_{L_2(\Omega)}$	$\|\mathbf{v}-\mathbf{v}^4\|_{L_2(\Omega)}$
Re= 100,**k** = 1			
0.1	3.41×10^{-3}	5.85×10^{-3}	5.53×10^{-3}
0.05	2.52×10^{-3}	3.32×10^{-3}	3.88×10^{-3}
0.025	1.52×10^{-3}	1.39×10^{-3}	1.66×10^{-3}
Re= 100,**k** = 2			
0.1	1.16×10^{-3}	2.97×10^{-3}	3.26×10^{-3}
0.05	7.96×10^{-4}	1.39×10^{-3}	1.56×10^{-3}
0.025	4.98×10^{-4}	6.16×10^{4}	7.74×10^{-4}
Re= 400,**k** = 1			
0.1	1.44×10^{-2}	2.88×10^{-2}	2.80×10^{-2}
0.05	1.01×10^{-2}	1.52×10^{-2}	1.64×10^{-2}
0.025	6.07×10^{-3}	5.27×10^{-3}	6.46×10^{-3}
Re= 400,**k** = 2			
0.1	6.71×10^{-3}	2.07×10^{-2}	1.82×10^{-2}
0.05	3.88×10^{-3}	9.40×10^{-3}	8.73×10^{-3}
0.025	2.12×10^{-3}	3.04×10^{-3}	3.40×10^{-3}
Re= 1000,**k** = 1			
0.1	4.59×10^{-2}	9.04×10^{-2}	8.44×10^{-2}
0.05	3.61×10^{-2}	6.29×10^{-2}	5.97×10^{-2}
0.025	1.94×10^{-2}	2.53×10^{-2}	2.55×10^{-2}
Re= 1000,**k** = 2			
0.1	4.34×10^{-2}	8.99×10^{-2}	8.22×10^{-2}
0.05	2.87×10^{-2}	5.89×10^{-2}	5.32×10^{-2}
0.025	1.18×10^{-2}	2.15×10^{-2}	1.99×10^{-2}

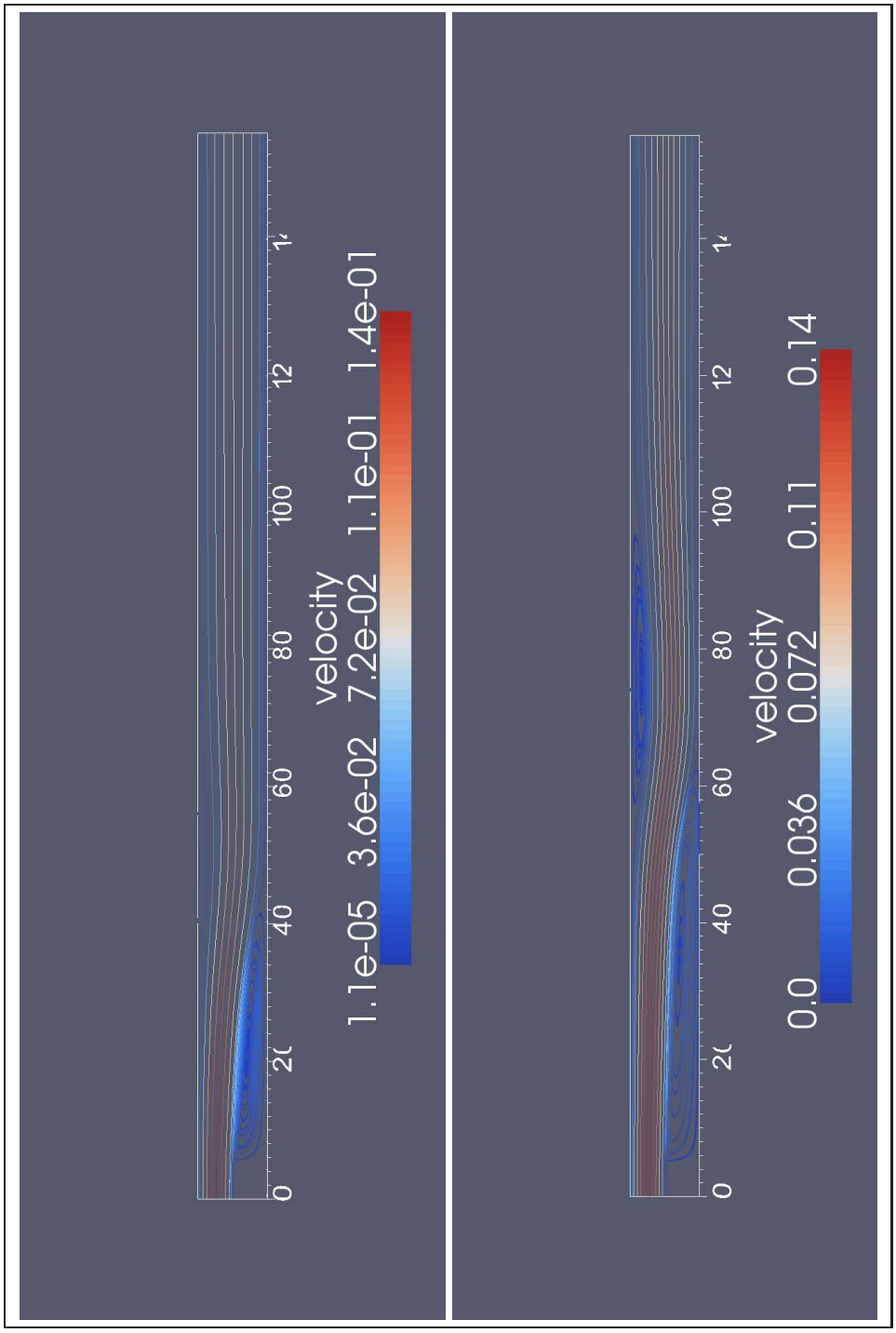

Figure 6. Backward facing step in 2D at Re = 400 and 800.

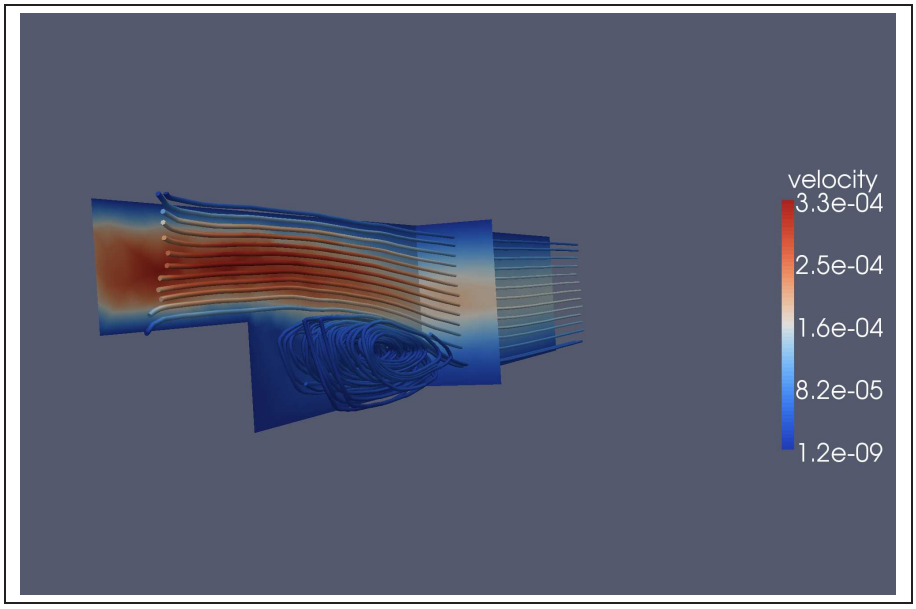

Figure 7. Backward facing step in 3D at Re = 1000.

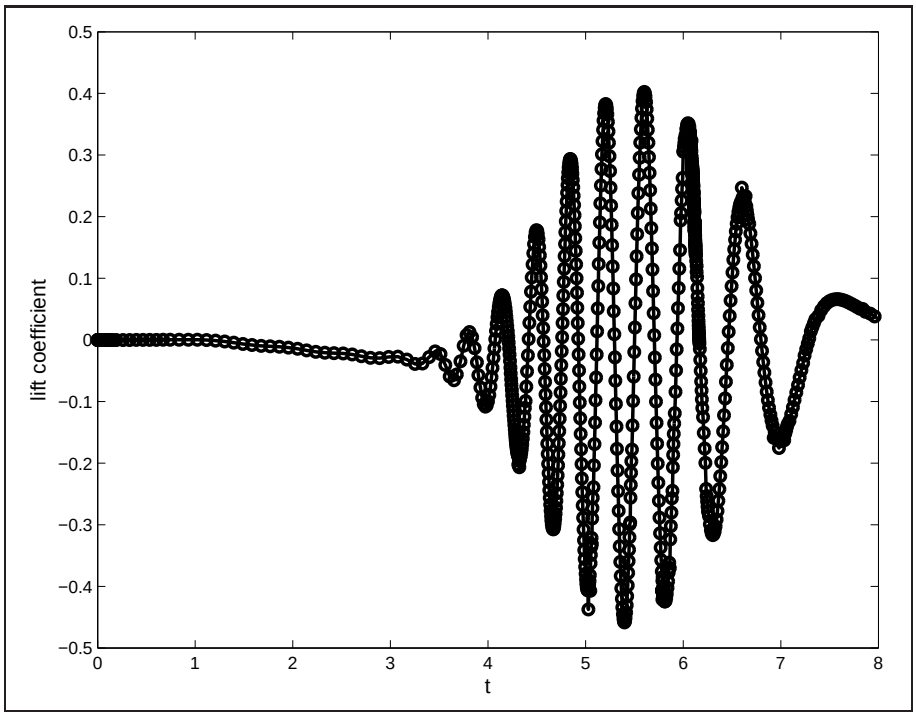

Figure 8. Lift coefficient versus time for 0 ≤ Re(t) ≤ 100.

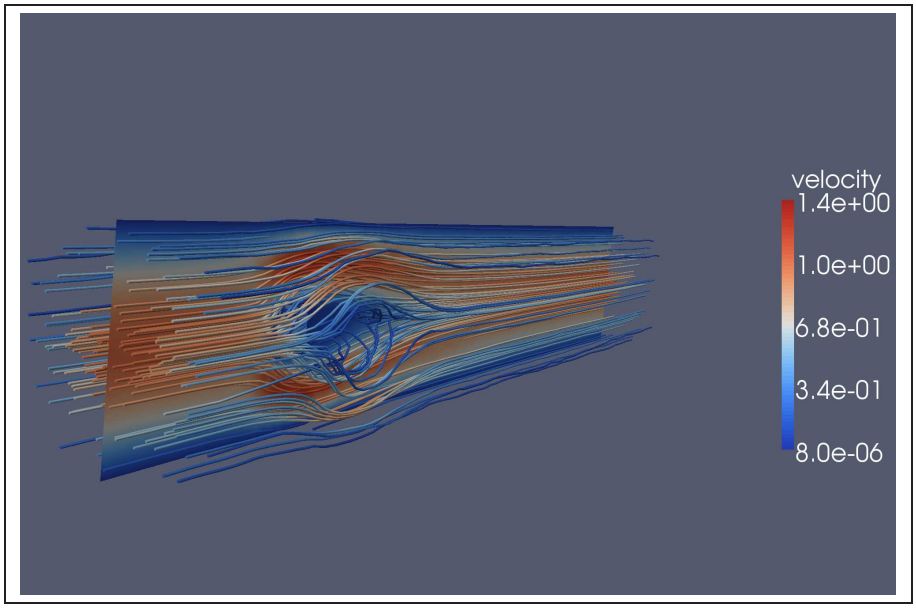

Figure 9. Flow around a square cylinder in 3D at Re = 70 .

5 Conclusions

We described a set of numerical methods for approximating widely used models of incompressible flow. The methods apply to complex geometries and unstructured meshes, provide locally conservative velocity fields, and achieve higher-order accuracy in space and time. Furthermore the multiscale variational method employed provides reasonable accuracy for high Re flows and has shown promise as a hybrid LES/DNS method (Hoffman and Johnson, 2006; Bazilevs et al., 2007). The methods and implementation were verified on a set of two- and three-dimensional benchmark problems. Several issues for future work were identified:

- **An alternative to the quasi-static subgrid scales assumption in the subgrid error approximation should be implemented for small times steps.**
- **Futher work on error estimation and startup heuristics are needed since spatial and temporal error are tightly coupled and error**
- **Work vs. error studies should be conducted to verify that the second-order methods are superior to first-order methods.**

References

Armaly, B. F., F. Durst, J. C. F. Pereira, and B. Schönung (1983). Experimental and theoretical investigation of backward-facing step flow. Journal of Fluid Mechanics 127, 473–496.

Ashcraft, C. and R. Grimes (1999). Spooles: An object-oriented sparse matrix library. In Proceedings of the 9th SIAM Conference on Parallel Processing for Scientific Computing.

Balay, S., K. Buschelman, V. Eijkhout, W. D. Gropp, D. Kaushik, M. G. Knepley, L. C. McInnes, B. F. Smith, and H. Zhang (2004). PETSc users manual. Technical Report ANL-95/11 - Revision 2.1.5, Argonne National Laboratory.

Balay, S., K. Buschelman, W. D. Gropp, D. Kaushik, M. G. Knepley, L. C. McInnes, B. F. Smith, and H. Zhang (2001). PETSc Web page. http://www.mcs.anl.gov/petsc.

Balay, S., W. D. Gropp, L. C. McInnes, and B. F. Smith (1997). Efficient management of parallelism in object oriented numerical software libraries. In E. Arge, A. M. Bruaset, and H. P. Langtangen (Eds.), Modern Software Tools in Scientific Computing, pp. 163–202. Birkhäuser Press.

Bassi, F., A. Crivellini, D. A. D. Pietro, and S. Rebay (2006). An artificial compressibility flux for the discontinuous Galerkin solution of the incompressible Navier–Stokes equations. Journal of Computational Physics 218, 794–815.

Batchelor, G. K. (1967). An Introduction to Fluid Dynamics. Cambridge.

Bazilevs, Y., V. M. Calo, J. A. Cottrel, T. J. R. Hughes, A. Reali, and G. Scovazzi (2007). Variational multiscale residual-based turbulence modeling for large eddy simulation of incompressible flows. Computer Methods in Applied Mechanics and Engineering 197, 173–201.

Bernard, R. S., P. V. Luong, and M. J. Sanchez (2007). Par3d: Numerical model for incompressible flow with applications to aerosal dispersion in complex enclosures. Technical Report TR-07-9, U.S. Army Engineer Research and Development Center.

Chorin, A. J. (1968). Numerical solution of the Navier–Stokes equations. Mathematics of Computation 22(104), 745–762.

Dawson, C., S. Sun, and M. F. Wheeler (2004). Compatible algorithms for coupled flow and transport. Computer Methods in Applied Mechanics and Engineering 193, 2565–2580.

Demmel, J. W., S. C. Eisenstat, J. R. Gilbert, X. S. Li, and J. W. H. Liu (1999). A supernodal approach to sparse partial pivoting. SIAM J. Matrix Analysis and Applications 20(3), 720–755.

Erturk, E., T. C. Corke, and C. Gökçöl (2005). Numerical solution of 2-d steady incompressible driven cavity flow at high Reynolds numbers. International Journal for

Numerical Methods in Fluids 48, 747–774.

Farthing, M. W. and C. E. Kees (2008). Implementation of discontinuous galerking methods for level set equations on unstructured meshes. Technical Note CHETN-XII-2, U. S. Army Engineer Research and Development Center, Coastal and Hydraulics Laboratory.

Farthing, M. W. and C. E. Kees (2009). Evaluating finite element methods for the level set equation. Technical Report TR-09-11, U. S. Army Engineer Research and Development Center, Coastal and Hydraulics Laboratory.

Farthing, M. W., C. E. Kees, T. S. Coffey, C. T. Kelley, and C. T. Miller (2003). Efficient steady-state solution techniques for variably saturated groundwater flow. Advances in Water Resources 26, 833–849.

Hoffman, J. and C. Johnson (2006). A new approach to turbulence modeling. Computer Methods in Applied Mechanics and Engineering 23-24, 2865–2880.

Hughes, T. (1995). Multiscale phenomena: Greens's functions, the Dirichlet-to-Neumann formulation, subgrid scale models, bubbles and the origins of stabilized methods. Computer Methods in Applied Mechanics and Engineering 127, 387–401.

Hutter, K. and K. D. Jöhnk (2004). Continuum Methods of Physical Modeling: Continuum Mechanics, Dimensional Analysis, Turbulence. Springer.

John, V., G. Matthies, and J. Rang (2006). A comparison of time-discretization/linearization approaches for the incompressible Navier–Stokes equations. Computer Methods in Applied Mechanics and Engineering 195, 5995–6010.

Kees, C. E., M. W. Farthing, and C. N. Dawson (2008). Locally conservative, stabilized finite element methods for variably saturated flow. Computer Methods in Applied Mechanics and Engineering 197(51-52), 4610–4625.

Kees, C. E., M. W. Farthing, and M. T. Fong (2009). Evaluating finite element methods for the level set equation. Technical Report TR-09-11, U. S. Army Engineer Research and Development Center, Coastal and Hydraulics Laboratory.

Knoll, D. A. and P. R. McHugh (1998). Enhanced nonlinear iterative techniques applied to nonequilibrium plasma flow. SIAM Journal on Scientific Computing 19(1), 291–301.

Larson, M. and A. Niklasson (2004). A conservative flux for the continuous Galerkin method based on discontinuous enrichment. CALCOLO 41, 65–76.

Oberkampf, W. L. and T. G. Trucano (2002). Verification and validation in computational fluid dynamics. Progress in Aerospace Sciences 33, 209–272.

Roache, P. J. (1998). Verification of codes and calculations. AIAA Journal 36(5), 696–702.

Schäfer, M., S. Turek, F. Durst, E. Krause, and R. Rannacher (1996). Benchmark computations of laminar flow around a cylinder. Notes on Numerical Fluid Mechanics 52, 547–566.

Williams, P. T. and A. J. Baker (1997). Numerical simulations of laminar flow over a backward-facing step. International Journal for Numerical Methods in Fluids 24, 1159–1183.

REPORT DOCUMENTATION PAGE

Form Approved
OMB No. 0704-0188

1. REPORT DATE *(DD-MM-YYYY)*	**2. REPORT TYPE**	**3. DATES COVERED** *(From - To)*
August 2009	Final Report	

4. TITLE AND SUBTITLE

Locally Conservative, Stabilized Finite Element Methods for a Class of Variable Coefficient Navier-Stokes Equations

5a. CONTRACT NUMBER

5b. GRANT NUMBER

5c. PROGRAM ELEMENT NUMBER

6. AUTHOR(S)

C.E. Kees, M.W. Farthing, and M.T. Fong

5d. PROJECT NUMBER

5e. TASK NUMBER

5f. WORK UNIT NUMBER
KHBCGD

7. PERFORMING ORGANIZATION NAME(S) AND ADDRESS(ES)

U.S. Army Engineer Research and Development Center
Coastal and Hydraulics Laboratory
3909 Halls Ferry Road
Vicksburg, MS 39180-6199

8. PERFORMING ORGANIZATION REPORT NUMBER

ERDC/CHL TR-09-12

9. SPONSORING / MONITORING AGENCY NAME(S) AND ADDRESS(ES)

10. SPONSOR/MONITOR'S ACRONYM(S)

11. SPONSOR/MONITOR'S REPORT NUMBER(S)

12. DISTRIBUTION / AVAILABILITY STATEMENT
Approved for distribution; distribution is unlimited.

13. SUPPLEMENTARY NOTES

14. ABSTRACT

Computer simulation of three-dimensional incompressible flow is of interest in many navigation, coastal, and geophysical applications. This report is the the fifth in a series of publications that documents research and development on a state-of-the-art computational modeling capability for fully three-dimensional two-phase fluid flows with vessel/ structure interaction in complex geometries (Farthing and Kees, 2008; Kees et al., 2008; Farthing and Kees, 2009; Kees et al., 2009). It is primarily concerned with model verification, often defined as "solving the equations right" (Roache, 1998). Model verification is a critical step on the way to producing reliable numerical models, but it is a step that is often neglected (Oberkampf and Trucano, 2002). Quantitative and qualitative methods for verification also provide metrics for evaluating numerical methods and identifying promising lines of future research.

(continued next page)

15. SUBJECT TERMS

Backward difference formulas	Computational fluid dynamics	Model verificatoin
Backward facing step	Driven cavity	Reynolds averaging
	Finite elements	Variational multiscale methods

16. SECURITY CLASSIFICATION OF:			**17. LIMITATION OF ABSTRACT**	**18. NUMBER OF PAGES**	**19a. NAME OF RESPONSIBLE PERSON**
a. REPORT	**b. ABSTRACT**	**c. THIS PAGE**			**19b. TELEPHONE NUMBER** *(include area code)*
UNCLASSIFIED	UNCLASSIFIED	UNCLASSIFIED		35	

Abstract (continued)

Fully-three dimensional flows are often described by the incompressible Navier-Stokes (NS) equations or related model equations such as the Reynolds Averaged Navier Stokes (RANS) equations and Two-Phase Reynolds Averaged Navier-Stokes equations (TPRANS).We will describe spatial and temporal discretization methods for this class of equations and test problems for evaluating the methods and implementations. The discretization methods are based on stabilized continuous Galerkin methods (variational multiscale methods) and discontinous Galerkin methods. The test problems are taken from classical fluid mechanics and well-known benchmarks for incompressible flow codes (Batchelor, 1967; Chorin, 1968; Schäfer et al., 1996; Williams and Baker, 1997; John et al., 2006). We demonstrate that the methods described herein meet three minimal requirements for use in a wide variety of applications: 1) they apply to complex geometries and a range of mesh types; 2) they robustly provide accurate results over a wide range of flow conditions; and 3) they yield qualitatively correct solutions, in particular mass and volume conserving velocity approximations.